ChemElectroChem

Research Article
doi.org/10.1002/celc.202500119

Chemistry Europe
European Chemical Societies Publishing

www.chemelectrochem.org

Designing a Silicon-Dominant Anode with Graphitic Carbon Coating from Biomass for High-Capacity Li-Ion Batteries

Siri Gani,* Axel Schönecker, Esmaeil Adabifiroozjaei, Leopoldo Molina-Luna, Elias Vollert, Vittorio Marangon, Dominic Bresser, Anke Weidenkaff, Magdalena Graczyk-Zajac, and Ralf Riedel

Silicon-carbon (Si/C) composites are extensively studied as anode materials for lithium-ion batteries (LIBs), with carbon typically sourced from biomass precursors or petroleum byproducts to produce amorphous and graphitic carbon, respectively. However, the use of iron salt as an "activator" to induce graphitization in combination with silicon remains unexplored. In this study, biomass-derived carbon is graphitized using an Fe salt activator to evaluate its effectiveness as a silicon coating for high-capacity anodes. Structural analysis via X-ray diffraction, Raman spectroscopy, and transmission electron microscopy reveals the formation of graphite, predominantly in the form of carbon nanotubes. Electrochemical performance is assessed in both half-cell and full-cell configurations, demonstrating the presence of "activated" graphite enhances reversible capacity, electronic conductivity, and cycle life. These findings highlight low-temperature Fe-assisted graphitization of biomass-derived-carbon as a promising approach for developing high-performance LIB anodes.

1. Introduction

The rapid advancements in portable electronic devices, such as smartphones and laptops, alongside the burgeoning growth of electric vehicles (EVs) as a pivotal strategy against climate change, have resulted in a surge in demand for lithium-ion batteries (LIBs).[1] While graphite has long been the anode material of choice for LIBs, its intrinsic capacity of 372 mAh g limits its potential for applications that demand higher energy storage performance.[2] Consequently, there is a concerted global effort to identify and develop alternative anode materials with superior energy densities. Among the candidates, silicon stands out as a promising anode material due to its extraordinary theoretical electrochemical specific capacity of 3579 mAh g—over 10 times that of graphite.[3–9] Beyond its impressive capacity, silicon is abundant, being the second most prevalent element in the Earth's crust, and has a relatively low-cost, making it a favorable choice from both economic and supply chain perspectives.[10]

Despite these advantages, less than 10 wt% silicon is used in commercial LIB anodes, although this figure is anticipated to rise to 10%–20% by 2025.[11] The commercialization of silicon-dominant (>50%) anodes remains challenging due to significant drawbacks such as silicon's inherently low electronic conductivity ($\approx 10^{-3}$ S cm)[12,13] and its extensive volume expansion (>300%) during lithium alloying.[14] The low conductivity of silicon hampers lithium-ion diffusion, while the substantial volume changes lead to particle pulverization and instability in the solid-electrolyte interphase (SEI).[15,16] To address these challenges, several strategies have been developed. One approach involves nanosizing silicon particles to below the critical threshold of 150 nm, thereby mitigating volumetric fluctuations and enhancing lithium diffusion rates.[17,18] Another strategy focuses on the development of silicon-carbon composites, incorporating materials like carbon nanotubes, graphene, and graphite to stabilize the structure and improve the electronic conductivity of silicon.[19–23] While nanosized silicon effectively manages volume expansion, its production is costly and energy-intensive. Conversely, micrometer-sized silicon (μSi) is more affordable, with costs comparable to that of graphite.[3,24–26] Thus, further research

S. Gani, E. Adabifiroozjaei, L. Molina-Luna, A. Weidenkaff, M. Graczyk-Zajac, R. Riedel
Materials Science
Technical University of Darmstadt
64287 Darmstadt, Germany
E-mail: siri.gani@tu-darmstadt.de

A. Schönecker
E-magy B.V.S
Bijlestaal 54A, 1721 PW Broek op Langedijk, Netherlands

E. Vollert, V. Marangon, D. Bresser
Helmholtz Institute Ulm (HIU)
Helmholtzstrasse 11, 89081 Ulm, Germany

E. Vollert, V. Marangon, D. Bresser
Karlsruhe Institute of Technology (KIT)
P.O. Box 3640, 76021 Karlsruhe, Germany

D. Bresser
Ulm University (Ulm)
89069 Ulm, Germany

M. Graczyk-Zajac
EnBW Energie Baden-Württemberg AG
Durlacher Allee 93, 76131 Karlsruhe, Germany

Supporting information for this article is available on the WWW under https://doi.org/10.1002/celc.202500119

is essential to optimize the use of μSi with a protective carbon layer, aiming to achieve high capacity at a competitive cost level. Currently, there has been a plethora of research on Si/C composites, and with the need for sustainability, biomass as a carbon precursor has come into spotlight, as it is widely available, cheap, and environmentally friendly.[27–30] This study focuses on the behavior of the Si/C composite with biomass as a carbon precursor and in the presence of a catalyst.

Carbon coating materials used in LIBs can be broadly categorized into two types: soft carbons (graphitizing) and hard carbons (non-graphitizing). Soft carbons, derived from precursors like pitch and petroleum coke, can be graphitized at temperatures exceeding 2000 °C.[31] Due to their ability to form crystalline graphite, soft carbon precursors are predominantly used as anode materials in LIBs. However, the high temperatures required for graphitization are energy-intensive and contribute to environmental degradation and greenhouse gas emission.[32] In contrast, carbons obtained from biomass precursors are typically amorphous, classified as hard carbons, and remain nongraphitizable even when subjected to extreme temperatures as high as 3000 °C.[33] A pathway for graphitizing hard carbons is the addition of transition metal salts (Fe, Ni, and Co salts) as "graphitization activators."[34–39] By this method, amorphous carbon can be transformed to crystalline graphite at temperatures above 700 °C.[40] Therefore, there is a growing need to develop graphite from a sustainable source such as biomass due to their worldwide abundance, ease of processing and low cost.[41,42] Across the literature, activated graphitization using a variety of transition metal salts, operated at a range of temperature, is reported.[43,44] Frankenstein et al. investigated the impact of different iron salts on the activation of carbon and reported that pure Fe metal is best suitable for inducing graphitization as Fe is in its reduced form and mobile to move through amorphous carbon.[44] He also studied the effect of concentration of Fe salt in "activating" carbon.[34] His studies concluded that the degree of graphitization increases with an increase in temperature and the concentration of Fe salt. Most of the research conducted on inducing graphitization in carbon obtained from biomass focuses on carbon anode.[45–47] However, the influence of Si as the active material with this type of "activated" graphite as the protective layer is less explored. Building on the well-established capacity enhancements achieved through silicon integration, this study further investigates the impact of "activated" graphite carbon-coated silicon as an anode material. Understanding this effect is crucial for advancing the development of more sustainable Si/C anodes with higher capacities for lithium-ion batteries.

In this study, we demonstrate the performance of silicon dominant anode with "activated" graphite as a protective layer in LIBs. Microporous silicon was employed as the active electrode material, while cellulose, a biomass precursor, served as the carbon source. The cellulose underwent change in carbon structure from amorphous to graphitic carbon through the addition of iron nitrate nonahydrate as an "activator." The resulting graphitic carbon coating enhances the material's reversible discharge capacity, thereby improving both the efficiency and cycle life of the anode. Additionally, this approach contributes to higher rate performance, further boosting the overall performance of the silicon-based anode.

2. Results and Discussion

2.1. Structure of the Si/C Composites

The crystalline phases of the synthesized composites were investigated through X-ray diffraction (XRD) measurements, as illustrated in Figure 2, S1, and S2, Supporting Information. **Figure 1**a displays the XRD patterns for the various samples (Si, p_Si/C, p_(G)Si/C+Fe, p_(G)Si/C), all exhibiting sharp reflexes at 13°, 21°, 25°, 30°, 33°, 37°, and 39°. These reflexes correspond crystalline silicon, indicating that the silicon's crystallinity was preserved during pyrolysis. The intensity of the Si reflections is significantly higher than that of carbon because of the high amount of Si present in the composite (silicon-dominant anode material). The inset

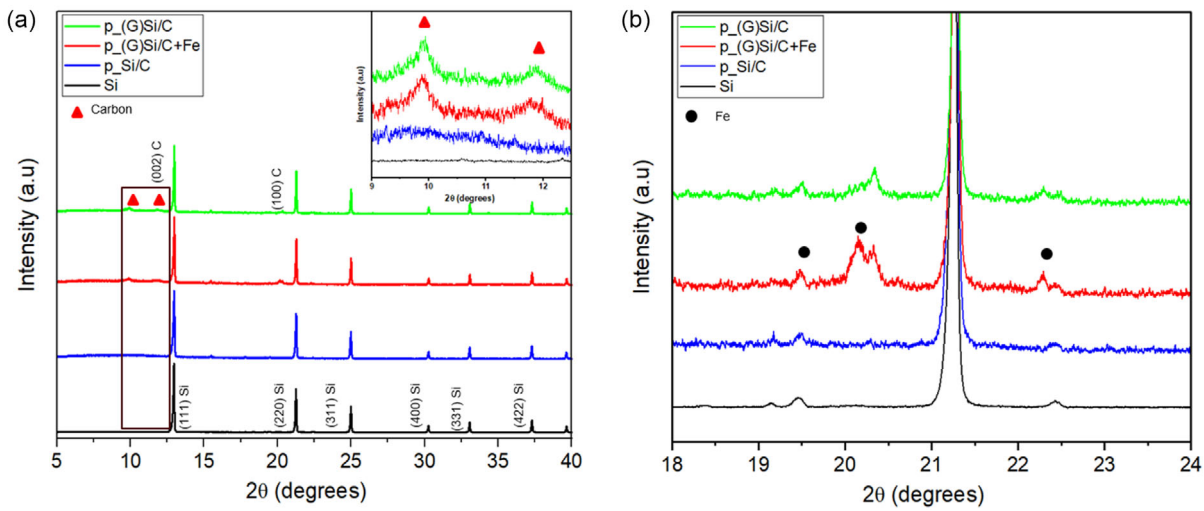

Figure 1. X-ray powder diffraction patterns of Si, p_Si/C, p_(G)Si/C+Fe, and p_(G)Si/C. a) Carbon peaks identified with star. b) Fe peaks identified with circle.

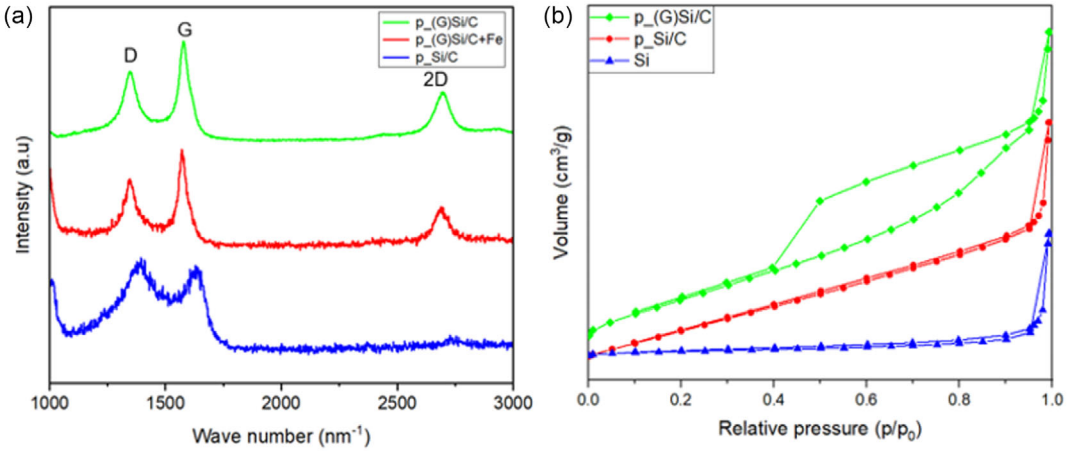

Figure 2. a) Raman spectra of p_Si/C, p_(G)Si/C+Fe, and p_(G)Si/C from 1000-3000 cm^{-1} highlighting only carbon peaks. b) Nitrogen adsorption isotherms of Si, p_Si/C, and p_(G)Si/C.

of **Figure 2**b focuses on the carbon peaks of the samples. The peak at 10° arises only in the presence of the "activator" which suggests the formation of rotationally arranged graphite. The absence of peak at 12.1° in p_Si/C confirms that it remains amorphous, while the presence of the peak in p_(G)Si/C+Fe and p_(G)Si/C indicates that iron acts as an activator for graphitization. Notably, the graphitic peak of p_(G)Si/C+Fe and p_(G)Si/C shifts to a lower angle (11.9°) compared to commercial graphite (12.1°). The interplanar distance, calculated using Bragg's equation ($n\lambda=2d\ \sin\theta$) is found to be 0.342 nm. This value suggests graphitization and formation of turbostratic carbon, characterized by rolled out graphene layers, hinting toward formation of carbon nanotubes (CNTs).[34,38,48] The CNTs are further discussed in TEM section. The degree of graphitization, calculated by the equation, $g = 0.344\text{-}d_{(002)}/0.086$, was determined to be 21% and the remaining 79% is amorphous carbon.[33] The additional reflections present in Figure 2b for the graphitized carbon-coated silicon anode are arising from Fe. After the leaching step, the intensity of the Fe-related peaks diminishes, indicating a partial removal of Fe. However, since some Fe reflections are still present in p_(G)Si/C, further research is required to achieve complete removal of the metal.

Figure S1, Supporting Information, presents the XRD patterns for different concentrations of Fe salt in combination with the Si/C composite. At 10 wt% Fe salt, no distinct peaks were found, indicating that the carbon remains amorphous at this concentration. However, a broad peak corresponding to carbon at 11.9° (002 plane) becomes evident in the presence of a 20 wt% Fe salt concentration, indicating the successful conversion of amorphous carbon into graphitic carbon. Hence, a 20 wt% Fe salt concentration was selected for further analysis, and all subsequent results pertain to this concentration. Figure S2, Supporting Information, shows minimal structural changes in the p_(G)Si/C+Fe samples with further increases in temperature up to 1000 °C. Thus, 800 °C was selected as the optimal temperature for the pyrolysis of the samples.

Raman spectroscopy was conducted to assess the graphitic structure of the carbon materials. The Raman spectra in Figure 2a, spanning the range of 1000–3000 cm^{-1}, focuses on the characteristic carbon bands. The three prominent peaks located at 1350 cm^{-1} (D band, indicative of disordered carbon), 1620 cm^{-1} (G band, associated with ordered carbon), and 2700 cm^{-1} (2D band, related to the stacking order of graphene layers) confirm the presence of carbon.[49] The relative intensities of the D and G bands, represented by the ratio I_D/I_G serve as a metric for the degree of graphitization. These intensities are obtained after fitting the Raman data in Figure S3, Supporting Information. Specifically, an $I_D/I_G > 1$ signifies a high degree of disorder within the carbon structure, while an $I_D/I_G < 1$ indicates a more ordered carbon framework.[50] For the p_Si/C material, the D band is notably broad and exhibits higher intensity than the G band, highlighting the amorphous nature of the carbon. Conversely, in the presence of an "activator," the G band intensity increases relative to the D band, accompanied by narrowing of the G band's width. This shift suggests the formation of graphitic carbon within the material.

The degree of graphitization (DoG) and the crystallite size (L_a) were calculated using Equation (1) and (2).[51] The DoG increased by 22% (from 33% for p_Si/C to 55% for p_(G)Si/C), and it remains unaffected by the leaching process. These findings are consistent with those obtained from the XRD analysis. The narrowing of G band aligns with an increase in L_a from 6.12 for p_Si/C to 8.34 nm for p_(G)Si/C+Fe which validates the conversion of carbon. Similar values were observed by Amel et al. for growing graphene from biochar.[52] Furthermore, the I_{2D}/I_G ratio offers critical insights into the nature of the graphitic material, particularly concerning the number of graphene layers and the stacking order. For both p_(G)Si/C+Fe and p_(G)Si/C, the I_{2D}/I_G ratio is less than 1, implying the presence of multilayer graphene structure.

$$DoG = \frac{I_G}{I_{D1} + I_G} \tag{1}$$

$$L_a = 2.4.10^{-10}.\lambda^4\left(\frac{I_G}{I_{D1}}\right) \tag{2}$$

Nitrogen physisorption data of all anodes shown in **Figure 3**b belong to a hybrid of type II and type IV isotherms with hysteresis

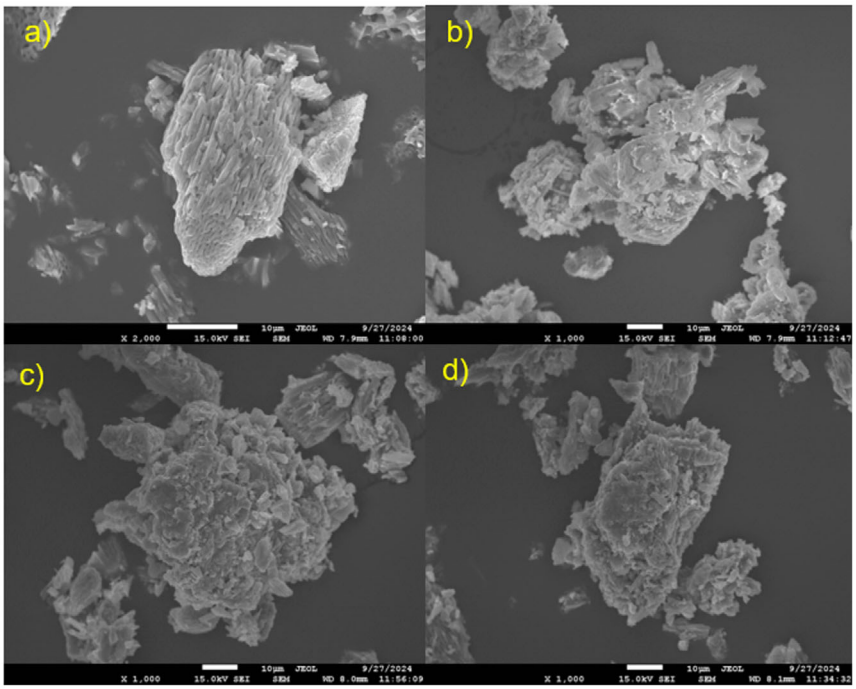

Figure 3. SEM images of a) bare Si, b) p_Si/C (before graphitization), c) p_(G) Si/C+Fe (after graphitization), and d) p_(G)Si/C (after leaching).

loop.[53] The hysteresis loop for p_(G)Si/C is a hybrid of H2 and H3, attributing to narrow pore heads and large cavitation holes.[54] The increase in N_2 consumption at higher pressures is an indication of macrospores in all of the anodes. Along with this, mesopores are also formed which is seen by the capillary condensation. The specific surface area (SSA) of bare Si amounts to 4.4 m^2 g. With the addition of carbon, the SSA increases to 43 m^2 g in p_Si/C due to the formation of pores during decomposition of cellulose to form porous carbon. The SSA of p_(G)Si/C after the leaching step increases to 51.2 m^2 g. This increase is related to the generation of new pores due to removal of Fe particles.[46]

The weight percentages of carbon and iron (Fe) were determined through elemental analysis, while the silicon (Si) content was calculated as the remaining fraction. Initially, Fe was introduced at 6 wt%, of which 2 wt% remained after the leaching process. Elemental analysis of the silicon–carbon composites (p_Si/C and p_(G)Si/C+Fe) measured an initial 18 wt% carbon composition, confirming the silicon-dominant nature of the material (76 wt% Si). After leaching, the carbon content increased to 20 wt%, while the Si content adjusted to 78 wt%, further validating the material's composition and removal of Fe. All relevant parameters are summarized in **Table 1**.

The scanning electron microscopy (SEM) image of bare/uncoated porous silicon is seen in Figure 3a. The morphology of carbon coated silicon with (p_(G)Si/C+Fe, p_(G)Si/C) and without (p_Si/C) the "activator" is similar, and the images showcase that carbon is well dispersed on the silicon surface, through Figure 3b–d. The EDAX results in Figure S4, Supporting Information, support the uniform distribution of carbon on silicon and the amount of iron (Fe) retrieved after leaching (2.81%) listed in Figure S5, Supporting Information, matches the analysis from elemental analysis. The high-resolution transmission electron microscopy (HRTEM) images in **Figure 4**a,b clearly show the silicon particles embedded in carbon matrix. The curved pattern seen in Figure S6, Supporting Information, features the "activator" enclosed in carbon shells.[55] The formation of rounded carbon is proof of turbostratic carbon with multiple layers of graphene. Under heat treatment, the "activator" travels through amorphous carbon and precipitates as graphitic carbon and in the process forms multiwalled CNTs (MWCNTs).[56]

2.2. Electrochemical Performance

The electrochemical performance of bare silicon (Si) and carbon-coated silicon composites (p_Si/C and p_(G)Si/C) is presented in

Table 1. Physical and structural properties of bare Si and carbon coated Si.

Sample	I_D/I_G	*DoG*	L_a [nm]	I_{2D}/I_G	BET [m^2/g]	C [%]	Fe [%]	Si [%]
Si	–	–	–	–	4.4	–	–	100
p_Si/C	1.14	33%	6.12	–	43.7	18	–	82
p_(G)Si/C+Fe	0.84	55%	8.34	0.87	–	18	6	76
p_(G)Si/C	0.87	55%	7.93	0.65	51.2	20	2	78

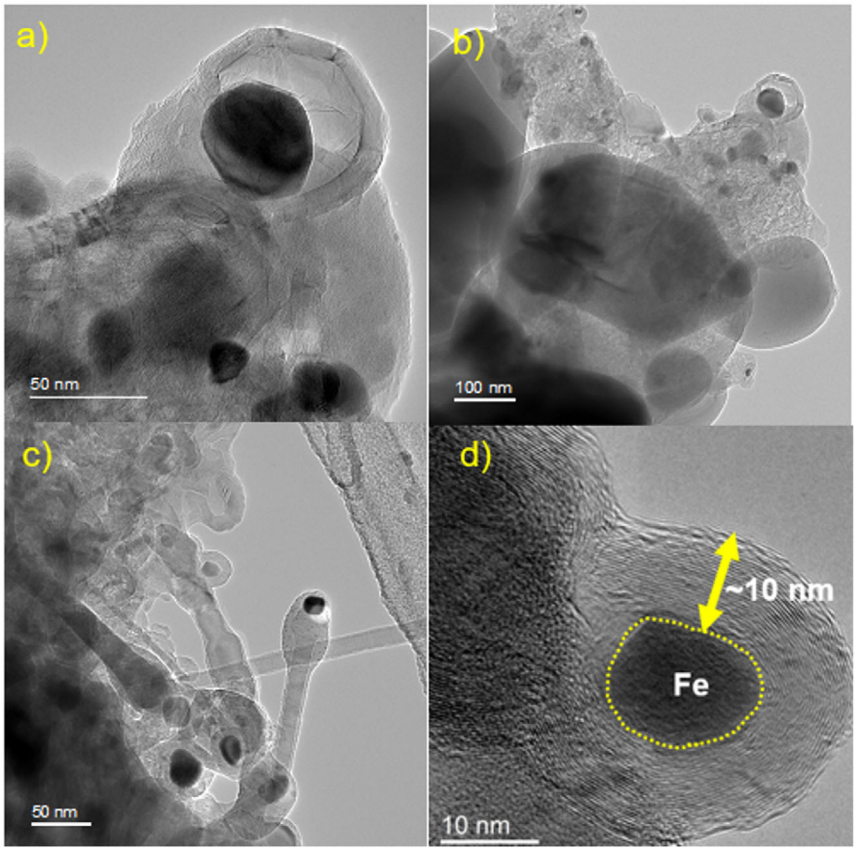

Figure 4. HRTEM images of a,b) p_Si/C (before graphitization) and c,d) p_(G) Si/C+Fe (after graphitization, without leaching).

Figure 5a). Due to the significant volumetric changes of silicon during lithiation and delithiation, reaching up to 300%, the capacity is limited to 1000 mAh g to reduce the stress on silicon.[26] This capacity remains higher than that of graphite (372 mAh g).[57] As shown in **Figure 6**a, all anodes exhibit a stable gravimetric capacity of 1000 mAh g. However, the bare Si anode requires multiple cycles to reach the maximum capacity, whereas p_Si/C and p_(G)Si/C achieve their full capacity more rapidly. This behavior is attributed to the expansion of silicon, which progressively exposes more active material to the electrolyte, leading to additional solid electrolyte interphase (SEI) formation and a subsequent drop in efficiency.[13] This trend is further reflected in Figure 5b, The initial coulombic efficiency (ICE) values are 80.97% for Si, 62.41% for p_Si/C, and 61.24% for p_(G)Si/C. These ICE values correlate with the specific surface area (SSA) of the materials, as detailed in Table 1. Bare Si, with an SSA of 4.4 m^2 g, exhibits the highest ICE, while p_Si/C (43.7 m^2 g) and p_(G)Si/C (51.2 m^2 g) display lower ICE due to their higher SSA. A larger SSA provides more active sites for lithium-ion trapping during SEI formation, leading to increased lithium consumption and reduced ICE.[58] Notably, p_(G)Si/C demonstrates the highest long-term stability and efficiency, with a final coulombic efficiency of 99.5%, indicating a more robust SEI and improved lithium-ion accessibility compared to the other anodes.[23] The graphitized carbon enhances elasticity, while the amorphous carbon provides mechanical strength, effectively maintaining the structural integrity of the composite throughout cycling.

Figure 5c shows the voltage profiles of the first cycle for all anodes (Si, p_Si/C, p_(G)Si/C). For the Si anode, lithiation begins at around 1.0 V, leading to phase transformations and the formation of Li-rich phases, with crystalline Si converting to amorphous Si at lower voltages.[13] The Si anode exhibits a sharp voltage drop as lithium is rapidly inserted, whereas p_Si/C and p_(G)Si/C show more gradual curves due to the distributed lithiation across both silicon and carbon components. The initial specific discharge capacities of p_Si/C and p_(G)Si/C are lower than that of bare Si, as the SSA is larger for carbon coated composites compared to that of Si. During the discharge process, the curvature at 0.3 V and 0.5 V stems from the de-alloying mechanism of lithium from Li_xSi phase.

Figure 5d highlights the rate performance of Si, p_Si/C, and p_(G)Si/C. The C-rate is indicated for each step to provide a clear understanding of the performance at varying discharge rates while fixing a constant C-rate for charging. The carbon-coated p_Si/C and p_(G)Si/C anodes exhibit superior performance compared to bare Si at higher C-rates of 2C, 3C, and 4C. This performance decline at higher C-rates is attributed to the kinetic limitations of lithium-ion diffusion, as reduced charge/discharge times limit the interaction between lithium ions and the active material. Despite this, all anodes demonstrate strong structural integrity. Importantly, p_(G)Si/C achieves the highest specific discharge capacity at 4C, reaching 300 mAh g, which corresponds to 30% of its initial capacity (1000 mAh g). This superior performance is credited to the extensive interconnected silicon–carbon

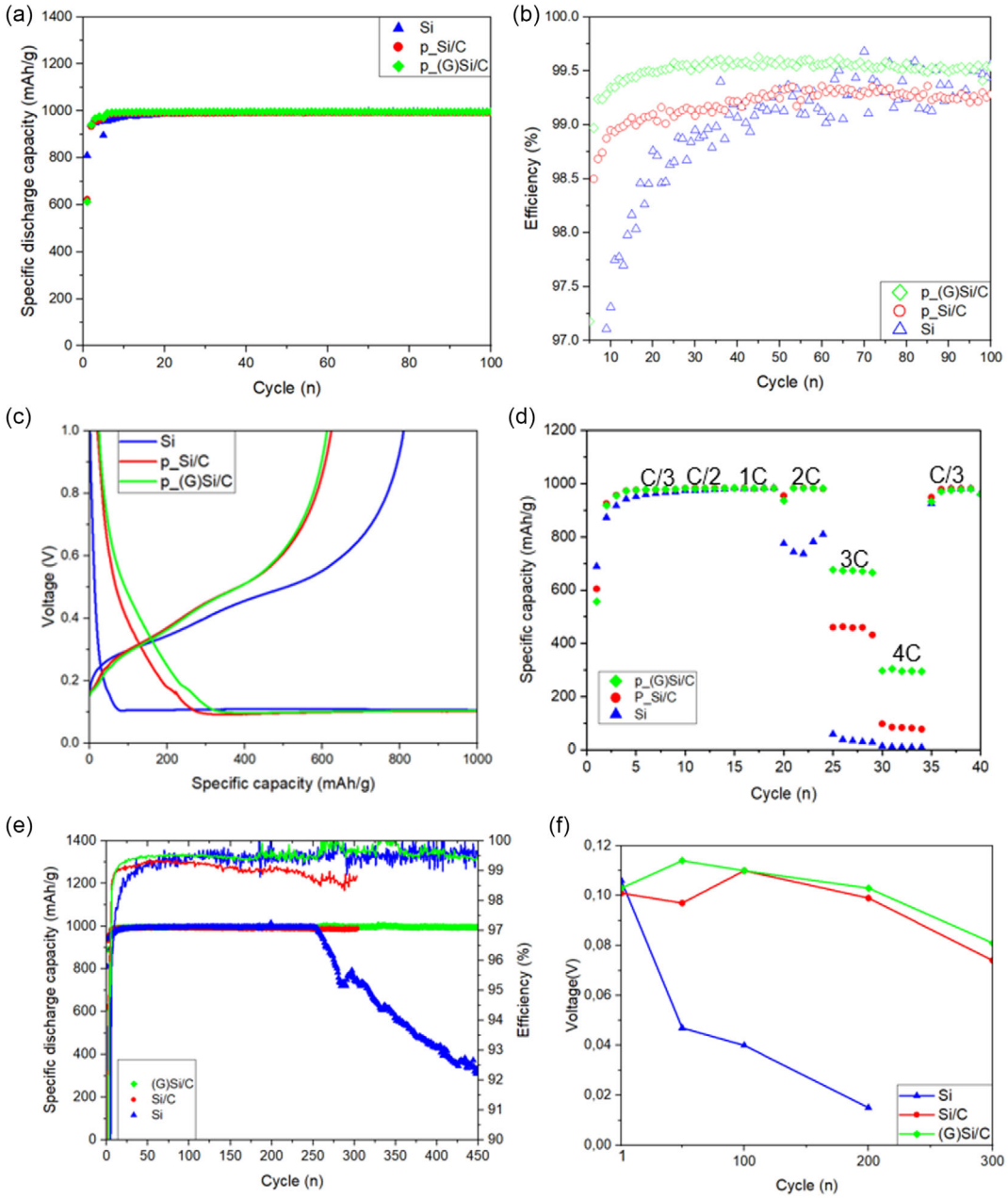

Figure 5. Half-cell cycling performance of Si, p_Si/C, and p_(G)Si/C. a) Specific gravimetric capacity. b) Efficiency after formation cycles. c) Galvanostatic charge/discharge profiles of first cycle at 0.2 C-rate. d) Rate performance at various C-rates displaying specific discharge capacity curves. e) Long cycle life. f) Voltage at the end of cycling for all anodes.

network that enhances electronic and ionic conductivity, facilitating efficient electron transport from each silicon particle.[59] Additionally, the porous carbon structure improves lithium-ion diffusion by facilitating better electrolyte infiltration, further optimizing performance.

The cycle life performance of the anodes is illustrated in Figure 5e. It is evident that the capacity of the bare Si anode deteriorates beyond 200 cycles, whereas the anodes incorporating carbon maintain a stable capacity. Figure 5f presents the voltage at different cycles. After 200 cycles, the bare Si anode reaches a low voltage of 0.01 V, while the p_Si/C and p_(G)Si/C anodes maintain voltages above 0.06 V. This indicates that in the bare Si anode, all the silicon is fully utilized, preventing further cycling. In contrast, the presence of carbon in the p_Si/C and p_(G)Si/C anodes ensures the availability of silicon, allowing for extended cycling stability.

Based on half-cell evaluations, the anodes follow the order of p_(G)Si/C > p_Si/C > Si in terms of cycle life and conductivity, highlighting the advantages of graphitized carbon in stabilizing silicon-based anodes for high-performance lithium-ion batteries.

To further assess the electrochemical performance of the anodes, full cells were assembled using the anodes paired with NMC cathodes, with a voltage window set between 3.0 and 4.0 V. The n/p ratio was chosen to be less than 1 (close to 0.99) to

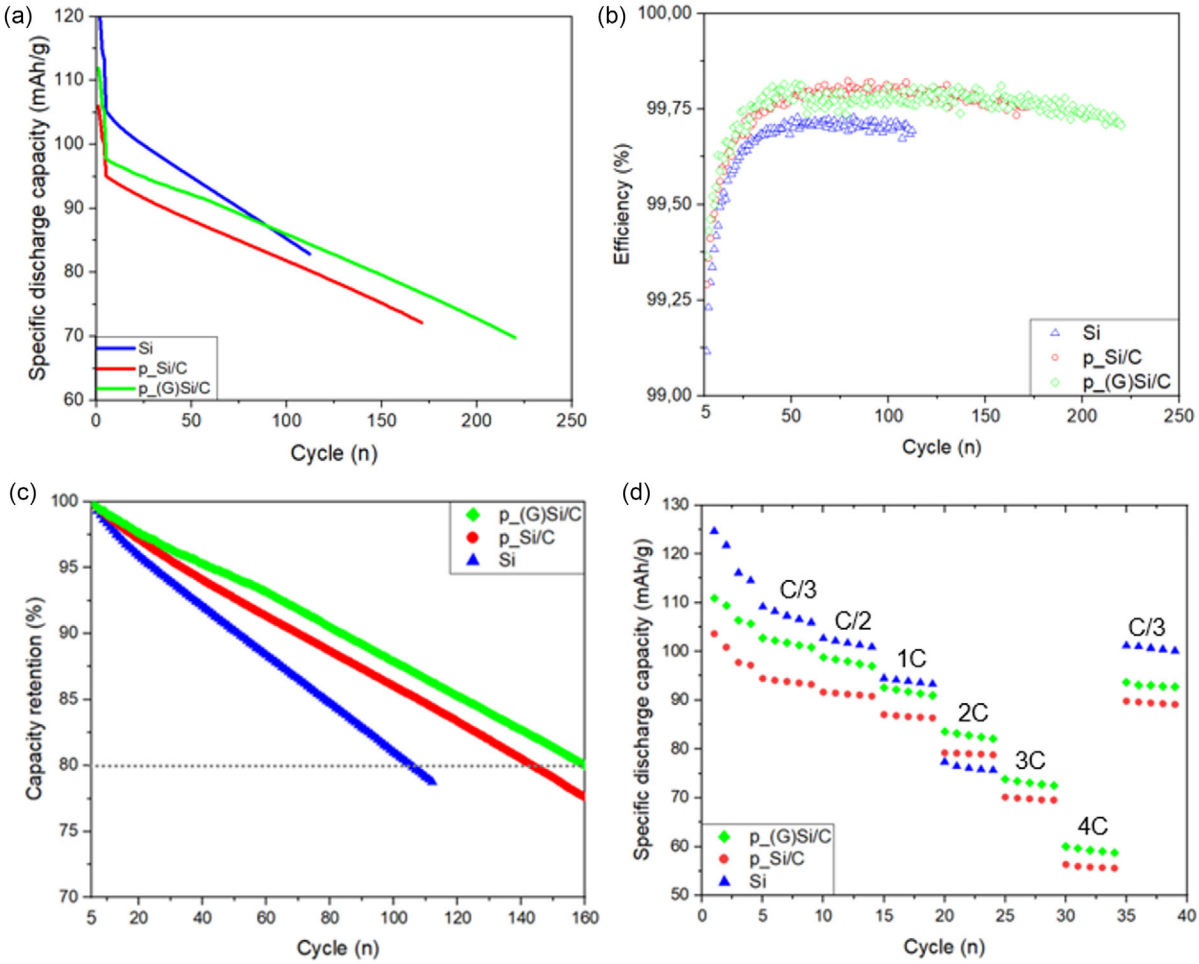

Figure 6. Full-cell cycling performance of Si, p_Si/C, p_Si/C (+5%), and p_(G)Si/C. a) Specific gravimetric capacity. b) Efficiency after formation cycles. c) Cycle life until capacity retention of 80%. d) Rate performance at various C-rates displaying specific discharge capacity curves.

account for the irreversible capacity losses associated with the SEI formation during the first cycle. The specific capacity is calculated based on the mass loading of the cathode. The discharge capacities of the cathodes paired up with Si, p_Si/C, and p_(G)Si/C are presented in Figure 6a. During initial testing at C/10, the Si, p_Si/C, and p_(G)Si/C cells exhibited first-cycle specific charge capacities of 168 mAh g, 167 mAh g, and 167 mAh g, respectively, with corresponding discharge capacities of 122 mAh g, 106 mAh g, and 105 mAh g. The observed initial capacity losses are attributed to irreversible Li-ion insertion during the formation of the SEI layer, resulting in capacity loss. The capacity of Si anode fades rapidly as Si is continuously exposed after each cycle. The slight improvement in the capacity of p_(G)Si/C is due to the formation of ordered graphite, which enhances ion transport between the two electrodes. As depicted in Figure 6b, the efficiency of the full cells closely mirrors that of the half cells, indicating minimal side reactions in the full cell configuration. The ICE for Si, p_Si/C, and p_(G)Si/C are 72%, 63%, and 62%, respectively. The ICE of Si in a full-cell setup is lower than that of half-cell, which exhibits that there are unwanted side reactions when bare Si is used as an anode.

The cycle life, evaluated in terms of capacity retention (CR) after the formation cycles (starting from the 5th cycle), is illustrated in Figure 6c. The 80% capacity retention milestone was reached at 102 cycles for Si, 143 cycles for p_Si/C, and 160 cycles for p_(G)Si/C, demonstrating that the p_(G)Si/C anode provides significantly improved cycle life compared to both p_Si/C and Si. This enhanced durability is attributed to the interconnected silicon-carbon network, which helps mitigate capacity fading by maintaining effective electrical contact between silicon particles, thereby improving structural stability during cycling.

The rate capability tests were conducted first by increasing the discharge rate for the first 35 cycles, followed by returning to the initial discharge rate to assess the structural integrity and recovery capacity, as shown in Figure 6d. The Si anode was discharged up to 2C, while the carbon coated anodes were discharged up to 4C. The capacity of all anodes was recovered when the discharge rate was returned to C/3, indicating that the structure remains intact even after exposure to high discharge rates. Initially, the specific capacity of Si was the highest, and as the C-rate increased, the specific capacity of Si fell below Si/C composites. This fade in capacity is because of the lack of conductive network from carbon. The discharge specific capacity of Si at 2C is comparable to p_(G)Si/C at 3C (55% of initial capacity), demonstrating the enhanced rate capability of p_(G)Si/C.

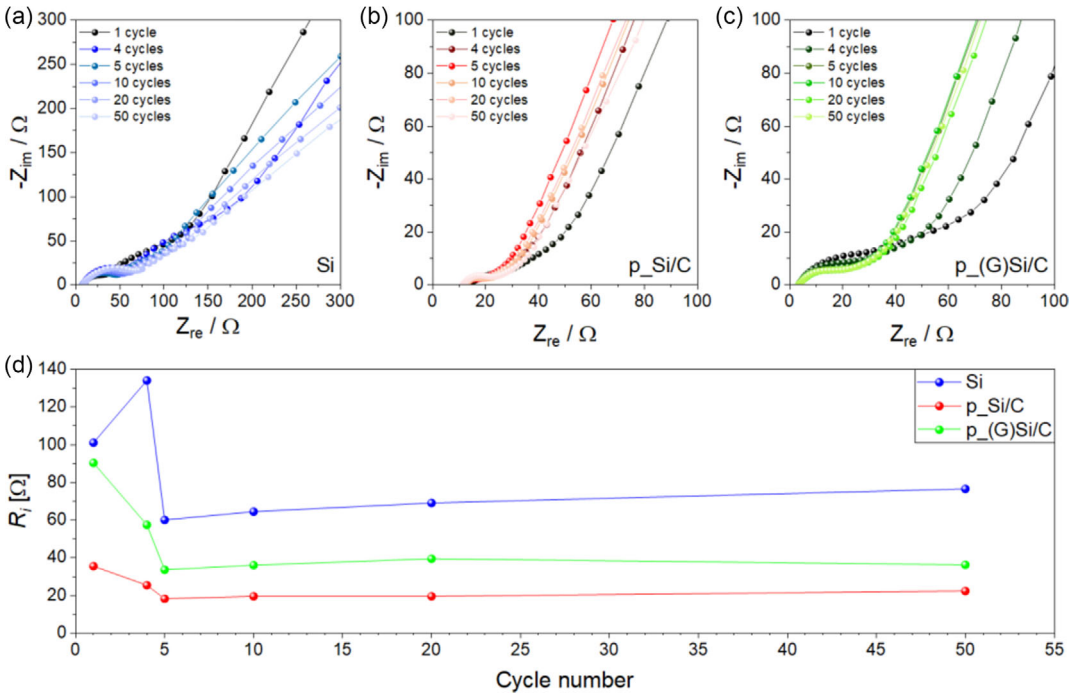

Figure 7. Nyquist plots recorded by EIS upon galvanostatic cycling on lithium cells. a) Si, b) p_Si/C or c) p_(G)Si/C electrode, and d) interface resistance of all electrodes.

These findings confirm that the presence of graphite in Si/C composite improves conductivity.

The stability of the electrode|electrolyte interface resistance (R_i) related to the Si, p_Si/C and p_(G)Si/C electrodes in lithium cell was evaluated by electrochemical impedance spectroscopy (EIS) performed upon cycling. **Figure 7** depicts the Nyquist plots recorded at the 1st, 4th, 5th, 10th, 20th, and 50th cycles for the Si (Figure 7a), p_Si/C (Figure 7b), and p_(G)Si/C (Figure 7c) electrodes, as well as the trend in function of the cycle number of R_i (Figure 7d) comprising contributes from the passivation layer and charge transfers as determined by nonlinear least squared (NLLS) fitting of the Nyquist plots (see actual values in Table S8, Supporting Information). The Si electrode shows in general the highest R_i values, exhibiting an increase from 101 to 134 Ω during the four activation cycles likely due to progressive lithiation of the Si particles with volume expansion and disruption of the native SEI layer, followed by a drop to 60 Ω after the first cycle at 0.5 A g^{-1} and by a slight growth to 77 Ω throughout the test in line with the reformation of a lowly resistive, yet growing, passivation layer. The p_Si/C and p_(G)Si/C present instead a different behavior characterized by the decrease of R_i during the 4 activation cycles from 36 to 25 Ω and from 90 to 57 Ω, respectively, showing subsequently rather constant values respectively around 20 and 35 Ω. The significant drop in R_i in p_(G)Si/C can be related to the presence of graphite and Fe. The relevant improvement in R_i exhibited by the p_Si/C and p_(G)Si/C electrodes with respect to the bare Si can be attributed to the optimization of the carbon matrix, which allows for the accommodation of the volume expansion upon lithiation of the Si particles and, consequently, for the formation of a stable and lowly resistive SEI. The enhanced carbon matrix of p_Si/C and p_(G)Si/C also justifies the lower initial R_i, in line with an improved ionic and electronic conductivity of the electrodes.

3. Conclusions

In this work, we investigated the structural and electrochemical properties of silicon–carbon (Si/C) composites with and without iron as an "activator" for graphitization. The motivation behind this work was to improve the structural integrity of a silicon-dominant anode material by incorporating graphitic carbon derived from biomass (cellulose). The resulting process involved key steps such as impregnating cellulose with Fe salt, heating the mixture at 800 °C, and then leaching to remove the formed iron nanoparticles. The X-ray diffraction (XRD) and Raman spectroscopy analyses revealed that the addition of iron significantly influenced the graphitization process, leading to the formation of graphite. The interplanar distance of carbon was reduced to 0.342 nm which implies formation of turbostratic carbon. Raman spectroscopy confirmed the presence of multiple graphene layers which suggests that the graphite formed is in the form of multi-walled CNT. The SSA increases in the presence of carbon, because of which the ICE of Si/C composites is lower than that of bare Si. "Activated" graphitization contributed to improved reversibility and electronic conductivity of the anode. The cycle life of anodes with carbon is significantly enhanced as carbon serves as a protective layer and preserves Si from fully being utilized. The interfacial resistance R_i is the lowest for Si, and the drop in R_i during the formation cycle of p_(G)Si/C is significant due to the presence of graphite. Future work is recommended to improve the ICE in a full cell by pre-lithiating the

anode to mitigate lithium loss during SEI formation. Moreover, the cycle life can be extended by introducing additional heating step after leaching and increasing the packing density.

4. Experimental Section

Synthesis of Si/C Composites

Micron sized macroporous Si (E-magy, Netherlands) and cellulose (microcrystalline cellulose powder, Sigma–Aldrich) were combined in an initial weight ratio of 2:3 (Si:cellulose) in absolute ethanol and deionized water with a ratio of 2:1 by volume, wherein the cellulose dissolves. This mixture was heated to 80 °C and stirred for 90 min to achieve a homogeneous dispersion. Subsequently, the temperature was increased to 90 °C and maintained until the solvent evaporated, resulting in the formation of a gel-like structure. The obtained composite was dried at 80 °C for 24 h. The dried Si/C composite was impregnated with 10, 15, and 20 wt% iron nitrate nonahydrate ($Fe(NO_3)_2 9H_2O$) in deionized water. The impregnation process was conducted at 80 °C for 4 h, followed by drying at 80 °C for an additional 24 h. This composite is referred to as Si/C+Fe. The Si/C+Fe composite underwent pyrolysis in argon atmosphere at temperatures ranging between 800 °C and 1000 °C with a heating rate of 100 °C/min and a holding time of 3 h at the peak temperature. The resultant composite, after pyrolysis, was designated as p_(G)Si/C+Fe. The pyrolyzed p_(G)Si/C+Fe composite was leached using a 1M HCl solution (solid:liquid = 1 g:20 mL) at 80 °C for 2 h to remove the iron particles. The leached solution was then filtered using Buchner filtration and washed with deionized water to ensure complete removal of residual acid (referred as p_(G)Si/C). For comparison, a Si/C composite was prepared without the addition of Fe salt as the reference sample. This composite underwent the same pyrolysis process (800 °C) to form p_Si/C, but did not undergo the leaching step. All obtained samples (p_(G)Si/C and p_Si/C) were dry sieved to achieve a particle size below 45 μm. These materials were then used for the electrode preparation.

Microstructure Characterization

The morphology of the samples was examined using SEM with a JEOL JSM-7600 F microscope. XRD analysis was conducted on a Bruker D8 diffractometer using Mo Kα radiation ($\lambda = 0.154$ nm) to investigate the phase structure and estimate the interplanar distance of the graphitized carbon, covering the 2θ range of 5–40 degrees. Raman spectroscopy was performed using a Horiba HR800 spectrometer with a 532 nm excitation wavelength, spanning the range of 1000-3500 cm^{-1}. The specific surface area and pore size distribution were determined through N_2 adsorption measurements at 77 K using an Autosorb 3B analyzer. Samples were degassed at 250 °C for 24 h prior to the measurements. The carbon content was measured by burning the sample using a carbon analyzer from Leco.

Electrochemical Tests

The active materials (Si, p_Si/C, p_(G)Si/C) after sieving <45 μm were mixed with graphite (TIMCAL Graphite & Carbon), carbon black (Super P) as the conductive additives, and polyacrylic acid (PAA with buffer solution, Sigma–Aldrich) as the binder in a weight ratio of 75:5:10:10 to form a homogeneous slurry (IKA T25). This slurry was coated onto copper foil, which served as the current collector, using a doctor blade. The coated foils were dried at 80 °C for one h. The thickness of the electrode was adjusted to achieve an anode loading of 2-3 mg cm^2. Circular electrodes of 10 mm diameter were then punched out and dried under vacuum at 80 °C for 24 h in a Büchi B-585 glass oven.

Both half and full cells were assembled in an argon-filled glove box to prevent moisture and oxygen contamination. The cells were assembled and measured in Swagelok cells at 25 °C. In the half-cell configuration, the prepared anodes (Si, p_Si/C, p_(G)Si/C) were paired with lithium foil discs of 7.5 mm (Guangdong Canrd New Energy Technology Co., Ltd) as the counter electrode. The electrolyte comprised of 45 μL of 1 M x_6 in EC:EMC (30:70, by wt.) + 10 wt% FEC. A porous Whatman glass fiber membrane with a 14 mm diameter served as the separator. Electrochemical properties were tested using Neware battery testing systems. The cycling protocol included an initial rate of C/10 for the first four cycles, followed by C/2 for the subsequent cycles, with a voltage window of 0.01–1.0 V (1C = 1000 mAh g). Gravimetric capacity values correspond to the amount of silicon, measured in grams, present in the anode composition. In a limited capacity approach, each lithiation step is constrained to 1000 mAh g during subsequent cycles. Testing in a half-cell configuration continues for up to 100 cycles.

For the full cells, the cathode used was NMC622 with a 10 mm diameter. The theoretical capacity and areal loading of the cathode were 140 mAh g and 2 mAh cm^2, respectively. To emphasize the effect of the anode, the ratio of the negative to positive electrode (n/p) was chosen to be smaller than 1. The full cells were cycled between 3.0 V and 4.0 V. The full cells followed the cycling protocol of C-rate of C/10 for the first two cycles, followed by C/5 for the next two cycles, and C/2 for the remaining cycles. Full cell testing is presented until the capacity reaches at least 80% of the initial capacity (relative capacity measured after formation).

The rate capability was tested by maintaining a constant C-rate while charging and increasing the C-rate for discharge in the sequence of C/5 (formation cycle), C/3, C/2, 1C, 2C, 3C, 4C, and returning to C/3. Cyclic voltammetry (CV) measurements were performed using a VMP multipotentiostat (BioLogic Science Instrument), scanning at 0.05 mV/s between 0.01 V and 1.0 V for five cycles.

The capacity from silicon and carbon is calculated as follows

$$\text{Capacity\_total} = (W_{Si}.C_{Si}) + (W_C.C_C) \quad (3)$$

$$W_{Si} = 0.82\,(82\,\text{wt\%}),\ W_C = 0.18\,(18\,\text{wt\%}) \quad (4)$$

$$\text{Capacity from carbon } (W_C.C_C) = 0.18 \times 372\,\text{mAh g} = 74.4\,\text{mAh g}$$

Since the capacity is limited to 1000 mAh g, the equation is as follows

$$1000\,\text{mAh/g} = (0.82 * C_{Si}) + (74.4\,\text{mAh/g}) \quad (5)$$

$$\text{Capacity from Si} = 1000 - 74.4 = 925.6\,\text{mAh/g} \quad (6)$$

EIS Tests

Three-electrode Swagelok cells were assembled by stacking the working electrode (12 mm diameter, Si, p_Si/C, p_(G)Si/C), a lithium foil as counter electrode (12 mm diameter) and an additional lithium foil as reference (10 mm diameter). The working and counter electrodes were separated by a 13-mm diameter Whatman GF/D glass fiber separator soaked with 200 μL of electrolyte. EIS was measured after the 1st, 4th, 10th, 20th, and 50th cycles in a frequency range between 500 kHz and 10 mHz using an alternate voltage amplitude of 10 mV. The Nyquist plots recorded by EIS were fitted through the nonlinear least squared (NLLS) method using the Boukamp software. The fitting allowed the representation of the cells through equivalent circuits composed of resistive (R) and capacitive (Q) elements arranged in

series and/or in parallel. In particular, the $R_e(R_1Q_1)(R_2Q_2)Q_w$ and $R_e(R_1Q_1)(R_2Q_2)Q_g$ circuits were used, where R_e is the electrolyte resistance identified by the high-frequency intercept of the plot with the *x*-axis, the R_n elements arranged in parallel with the Q_n elements ($n = 1$ or 2) identify the amplitude of the high-middle-frequency semicircles of which the sum define the electrode|electrolyte interface resistance (R_i), while Q_w and Q_g, indicated either by a tilted or a vertical line, represent the infinite Warburg-type Li^+ diffusion and the geometric capacitance of the cell, respectively. Only fitting with a χ^2 value lower than 10^{-3} were considered suitable.

Acknowledgements

The authors would like to thank M.Sc. Laura Feldman for the SEM pictures and Dr. Esmaeil Adabifiroozjaei and Prof. Dr. Leopoldo Molina-Luna for the TEM images.

Open Access funding enabled and organized by Projekt DEAL.

Conflict of Interest

The authors declare no conflict of interest.

Author Contributions

Siri Gani: designed and performed the experiments, and analyzed the data. **Axel Schönecker**: supplied E-magy's silicon material and supervised the project. **Esmaeil Adabifiroozjaei**, **Leopoldo Molina-Luna**: captured TEM images and helped in TEM analysis. **Elias Vollert**, **Vittorio Marangon**, **Dominic Bresser**: performed EIS measurements and analysis. **Anke Weidenkaff**, **Magdalena Graczyk-Zajac**, **Ralf Riedel**: supervised the project.

Data Availability Statement

The data that support the findings of this study are available in the supplementary material of this article.

Keywords: carbon coating · graphite · high capacity · li-ion batteries · silicon anode

[1] M. Lavigne Philippot, D. Costa, G. Cardellini, *J. Energy Storage* **2023**, *60*, 106635.
[2] X. Zhao, V.-P. Lehto, *Nanotechnology* **2021**, *32*, 42002.
[3] Y. H. Qing Liu, X. Yu, *Nano Res. Energy* **2022**.
[4] X. Chen, H. Li, Z. Yan, *Sci. China Mater.* **2019**, *62*, 1515.
[5] A. M. Wilson, B. M. Way, J. R. Dahn, *J. Appl. Phys.* **1995**, *77*, 2363.
[6] C. Yu, X. Tian, Z. Xiong, *J. Alloys Compd.* **2021**, *869*, 159124.
[7] Q. Wang, M. Zhu, G. Chen, *Adv. Mater. Deerfield Beach, Fla.* **2022**, *34*, e2109658.
[8] J. Kim, O. B. Chae, B. L. Lucht, *J. Electrochem. Soc.* **2021**, *168*, 30521.
[9] X. Jiao, J. Yin, X. Xu, *Adv. Funct. Mater.* **2021**, *31*.
[10] H. Chen, Z. Wu, Z. Su, *Nano Energy* **2021**, *81*, 105654.
[11] Anode Market Surges as Electric Vehicle Demand Skyrockets, EVMarketsReports.com **2023**.
[12] X. Zhao, V.-P. Lehto, *Nanotechnology* **2021**, *32*, 42002.
[13] G. O. Jun Lee, H.-Y. Jung, *Mdpi Inorg.* **2023**.
[14] J. Asenbauer, T. Eisenmann, M. Kuenzel, *Sustain. Energy Fuels* **2020**, *4*, 5387.
[15] S. He, S. Huang, S. Wang, *Energy Fuels* **2021**, *35*, 944.
[16] J. Guo, D. Dong, J. Wang, *Adv. Funct. Mater.* **2021**, *31*.
[17] X. Zhao, V.-P. Lehto, *Nanotechnology* **2021**, *32*, 42002.
[18] Z. Yan, J. Jiang, Y. Zhang, *Mater. Today Nano* **2022**, *18*, 100175.
[19] H. Cheng, J. G. Shapter, Y. Li, *J. Energy Chem.* **2021**, *57*, 451.
[20] P. Li, H. Kim, S.-T. Myung, *Energy Stor. Mater.* **2021**, *35*, 550.
[21] O. Naboka, C.-H. Yim, Y. Abu-Lebdeh, *ACS omega* **2021**, *6*, 2644.
[22] A. S. Poonam Sehrawat, C. M. J. Abid, *J. Power Sources* **2021**.
[23] Y. Ma, P. Guo, M. Liu, *J. Alloys Compd.* **2022**, *905*, 164189.
[24] F. Maroni, M. Spreafico, A. Schönecker, *J. Electrochem. Soc.* **2022**, *169*, 80506.
[25] Z. Z. Qiang Ma, Y. Zhao, *Energy Storage Mater.* **2021**, 768.
[26] D. Jantke, R. Bernhard, E. Hanelt, *J. Electrochem. Soc.* **2019**, *166*, A3881.
[27] A. Liu, T.-F. Liu, H.-D. Yuan, Y. Wang, Y.-J. Liu, J.-M. Luo, J.-W. Nai, X.-Y. Tao, *New Carbon Mater.* **2022**, *37*, 658.
[28] P. Molaiyan, G. S. Dos Reis, D. Karuppiah, C. M. Subramaniyam, F. García-Alvarado, U. Lassi, *Batteries* **2023**, *9*, 116.
[29] G. S. Dos Reis, P. Molaiyan, C. M. Subramaniyam, F. García-Alvarado, A. Paolella, H. P. De Oliveira, U. Lassi, *Electrochem. Commun.* **2023**, *153*, 107536.
[30] H. Ahmed, G. Simoes Dos Reis, P. Molaiyan, A. Lähde, U. Lassi, *Prog. Energy* **2025**, *7*, 22003.
[31] L. M. Romero Millán, A. C. Ghogia, C. E. White, *ACS Appl. Nano Mater.* **2023**, *6*, 3549.
[32] R. Y. Fredina Destyorini, Y. Irmawati, *Diamonds and Related Mater.* **2021**.
[33] N. C. Sunwen Xia, W. Lu, *J. Cleaner Prod.* **2021**.
[34] V. Hanhart, L. Frankenstein, J. Ramirez-Rico, *ChemElectroChem* **2022**, *9*.
[35] J. L. Lili Gai, Q. Wang, *J. Environ. Chem. Eng.* **2021**.
[36] S. Xia, H. Yang, W. Lu, *Energy* **2022**, *239*, 122262.
[37] A. Gomez-Martin, Z. Schnepp, J. Ramirez-Rico, *Chem. Mater.* **2021**, *33*, 3087.
[38] R. D. Hunter, J. L. Rowlandson, G. J. Smales, *Mater. Adv.* **2020**, *1*, 3281.
[39] S. Xia, N. Cai, J. Wu, *Fuel Process. Technol.* **2020**, *209*, 106543.
[40] W. J. Sagues, J. Yang, N. Monroe, *Green Chem.* **2020**, *22*, 7093.
[41] C. Jin, J. Nai, O. Sheng, *Energy Environ. Sci.* **2021**, *14*, 1326.
[42] M. Winter, T. Placke, J. Ramirez-Rico, *ACS omega* **2019**, *4*, 21446.
[43] S. Xia, H. Yang, S. Lei, *Energy* **2023**, *262*, 125415.
[44] L. Frankenstein, P. Glomb, J. Ramirez-Rico, *ChemElectroChem* **2023**, *10*.
[45] N. A. Banek, K. R. McKenzie, D. T. Abele, *Scientific Rep.* **2022**, *12*, 8080.
[46] Z. Shi, Y. Jin, T. Han, *Scientific reports* **2024**, *14*, 3966.
[47] L. Lower, S. C. Dey, T. Vook, *ChemSusChem* **2023**, e202300729.
[48] E. C. Hayward, G. J. Smales, B. R. Pauw, *RSC Sustain.* **2024**, *2*, 3490.
[49] P. K. Mubari, T. Beguerie, M. Monthioux, *J. Carbon Res.* **2022**, *8*, 4.
[50] Y. Meng, C. I. Contescu, P. Liu, *Wood Sci Technol* **2021**, *55*, 587.
[51] L. G. Cançado, K. Takai, T. Enoki, *Appl. Phys. Lett.* **2006**, *88*.
[52] A. C. Ghogia, L. M. Romero Millán, C. E. White, *ChemSusChem* **2023**, *16*, e202201864.
[53] M. Thommes, K. Kaneko, A. V. Neimark, *Pure Appl. Chem.* **2015**, *87*, 1051.
[54] S. Xia, N. Cai, W. Lu, *J. Cleaner Prod.* **2021**, *329*, 129735.
[55] R. D. Hunter, J. Ramírez-Rico, Z. Schnepp, *J. Mater. Chem. A* **2022**, *10*, 4489.
[56] S. J. Goldie, K. S. Coleman, *ACS Omega* **2023**, *8*, 3278.
[57] B. Wang, Y. Li, N. Wu, *New J. Chem.* **2023**, *47*, 11533.
[58] P. M. Jannes Müller, A. Kwade, *Mdpi Batteries* **2023**.
[59] H.-J. Shin, J.-Y. Hwang, H. J. Kwon, *ACS Sustain. Chem. Eng.* **2020**, *8*, 14150.

Manuscript received: March 24, 2025
Revised manuscript received: July 7, 2025
Version of record online: August 19, 2025